

LOCAL TADPOLE GALAXIES: DYNAMICS AND METALLICITY

J. SÁNCHEZ ALMEIDA^{1,2}, C. MUÑOZ-TUÑÓN^{1,2}, D. M. ELMEGREEN³, B. G. ELMEGREEN⁴,
AND J. MÉNDEZ-ABREU^{1,2}*Draft version February 19, 2013*

ABSTRACT

Tadpole galaxies, with a bright peripheral clump on a faint tail, are morphological types unusual in the nearby universe but very common early on. Low mass local tadpoles were identified and studied photometrically in a previous work, which we complete here analyzing their chemical and dynamical properties. We measure H α velocity curves of seven local tadpoles, representing 50 % of the initial sample. Five of them show evidence for rotation ($\sim 70\%$), and a sixth target hints at it. Often the center of rotation is spatially offset with respect to the tadpole head (3 out of 5 cases). The size and velocity dispersion of the heads are typical of giant HII regions, and three of them yield dynamical masses in fair agreement with their stellar masses as inferred from photometry. In four cases the velocity dispersion at the head is reduced with respect to its immediate surroundings. The oxygen metallicity estimated from [NII] $\lambda 6583$ /H α often shows significant spatial variations across the galaxies (~ 0.5 dex), being smallest at the head and larger elsewhere. The resulting chemical abundance gradients are opposite to the ones observed in local spirals, but agrees with disk galaxies at high redshift. We interpret the metallicity variation as a sign of external gas accretion (cold-flows) onto the head of the tadpole. The galaxies are low metallicity outliers of the mass-metallicity relationship. In particular, two of the tadpole heads are extremely metal poor, with a metallicity smaller than a tenth of the solar value. These two targets are also very young (ages smaller than 5 Myr). All these results combined are consistent with the local tadpole galaxies being disks in early stages of assembling, with their star formation sustained by accretion of external metal poor gas.

Subject headings: galaxies: abundances – galaxies: dwarf – galaxies: evolution – galaxies: formation – galaxies: kinematics and dynamics – galaxies: structure

1. INTRODUCTION

Tadpole galaxies consist of a large star-forming clump at one end (the *head*) and a long diffuse region to one side (the *tail*). This asymmetric morphology is rather common at high redshift but rare in the local universe. For example, tadpoles constitute 10% of all galaxies larger than 10 pixels in the Hubble Ultra Deep Field (UDF) (Elmegreen et al. 2007; Elmegreen & Elmegreen 2010), and they represent 6% of the UDF galaxies identified by Straughn et al. (2006) and Windhorst et al. (2006) using automated search algorithms. In contrast, Elmegreen et al. (2012b, hereafter Paper I) find only 0.2% tadpoles among the star-forming local galaxies of the Kiso survey by Miyauchi-Isobe et al. (2010). This decrease suggests the tadpole morphology to represent a common but transit phase during the assembly of some galaxies. Since local tadpole galaxies are very low mass objects compared to their high redshift analogues (Elmegreen et al. 2012b), the phase must be already over for the local descendants of high redshift tadpoles.

Another independent observation also suggests that the tadpole morphology characterizes a very early phase of evolution. From the point of view of their chemi-

cal content, Extremely Metal Poor (XMP) galaxies are the least evolved objects in the local universe (e.g., Pagel et al. 1992; Kunth & Östlin 2000; Izotov & Thuan 2004). They represent only 0.1% of the galaxies in an arbitrary nearby volume (e.g., Morales-Luis et al. 2011), but a significant fraction of these chemically primitive objects turn out to have tadpole or cometary shape ($\sim 75\%$; Papaderos et al. 2008; Morales-Luis et al. 2011). This association between low metallicity and tadpole shape suggests that they are attributes characteristic of very young systems.

The tadpole structure could have a variety of origins. Elmegreen & Elmegreen (2010) showed lopsided ring-like galaxies that would look like tadpoles if viewed edge-on. Tadpoles could also result from mergers or close galaxy-galaxy interactions (e.g., Baldwin et al. 1982; Corbin et al. 2005; Straughn et al. 2006; Windhorst et al. 2006; D’Onghia et al. 2010). However, this merger scenario cannot be the universal pathway to tadpole formation, at least not locally, since the class of dwarf local tadpoles tends to be relatively isolated (Campos-Aguilar et al. 1993; Kunth & Östlin 2000) and lacks obvious tidal features (Papaderos et al. 2008). Another possibility is that the lopsided starburst results from ram compression by motion through the intergalactic medium (Elmegreen & Elmegreen 2010). Tadpoles could be disks with star formation triggered on the leading side and the rest visible as a red tail of older stars. Alternatively, they could be heavily stripped galaxies with star formation and old stars at the leading edge, and a tail made from star formation in the

jos@iac.es, cmt@iac.es, elmegreen@vassar.edu, bge@us.ibm.com, jairo@us.ibm.com

¹ Instituto de Astrofísica de Canarias, E-38205 La Laguna, Tenerife, Spain² Departamento de Astrofísica, Universidad de La Laguna, Tenerife, Spain³ Department of Physics and Astronomy, Vassar College, Poughkeepsie, NY 12604, USA⁴ IBM Research Division, T.J. Watson Research Center, Yorktown Heights, NY 10598, USA

stripped gas (e.g., Chung et al. 2009). The scenario in which dwarf galaxies are converted into dwarf spheroidal galaxies in the halos of larger galaxies (Lin & Faber 1983; van den Bergh 1994; Mayer et al. 2006) or in galaxy clusters (Boselli et al. 2008; van Zee et al. 2004) could involve a tadpole phase as the gas and young stars are pulled behind. A third possibility is that some tadpoles are normal disk galaxies with a large turbulent Jeans length for gravitational collapse of their interstellar medium. This happens in galaxies that have either small rotational velocities or large turbulent motions, and in this case only large star forming clumps can be produced (Förster Schreiber et al. 2006; Elmegreen et al. 2009). If there is only one clump at any particular time, then it will appear as a tadpole viewed from the right perspective. A fourth possibility is that the head-tail structure results from propagating star formation across a disk (e.g., Franx et al. 1997; Papaderos et al. 2008). Finally, as we propose in this paper, the head of the tadpole may result from accretion of external flows of pristine gas, that penetrate the dark matter halo and hit and heat a pre-existing disk. Cosmological simulations predict cold-flow buildup to be the main mode of galaxy formation (Dekel et al. 2009; Genel et al. 2012), and the incoming gas is expected to form giant clumps that spiral in and merge into a central spheroid (Noguchi 1999; Genzel et al. 2008; Elmegreen et al. 2008). In addition, inflow of low-metallicity gas seems to be suggested by distorted HI velocities and morphologies of some local star-forming galaxies (see López-Sánchez et al. 2012, and references therein).

It is important to realize that the different formation mechanisms mentioned above are not mutually exclusive, but exhibit a large degree of overlap between them. For example, the cold-flow accretion may be considered as a (minor-)merger accretion, and it may also be regarded as the interaction of the galaxy with the (filamentary) intergalactic medium.

In this context of galaxy formation, we examined a sample of fourteen tadpole galaxies in the local universe for comparison with high-redshift tadpoles (Paper I). These local tadpoles seem to form a continuous sequence with the UDF tadpoles studied by Elmegreen & Elmegreen (2010). With regards to their photometric properties, local tadpoles occupy the low mass end in sequences such as star formation, surface density and mass-to-light ratio. In addition, the radial intensity profiles of the local tadpoles show an exponential decrease at large galactocentric distances, which was interpreted as evidence for an underlying disk. The work in Paper I is followed up in the present paper. In order to determine the dynamical properties and metallicities of local tadpoles, we measure $H\alpha$ spectra along the head-tail direction in a representative fraction of the original sample. The results reported here show the galaxies to be rotating structures with an unexpected metallicity pattern, which may shed light into the nature of the tadpole morphology.

The paper is organized as follows: Sect. 2 describes the observations, the main steps of the reduction, and the main properties of the resulting spectra. Section 3 details the approximations used along the work to derive physical parameters from spectra. Section 4 analyzes the dynamical properties of the galaxies, their rotation

curves (RCs) and linewidths. These are used to infer dynamical masses, which are then compared with the stellar masses derived in Paper I (Sect. 6). Section 5 studies the light profiles both in continuum and $H\alpha$ emission. The variation of the oxygen abundance along the galaxy is measured in Sect. 7. Notes on individual galaxies are given in Sect. 8. The results of our observation in the context of tadpoles as dynamically young disks are discussed in Sect. 9.

2. OBSERVATIONS AND DATA REDUCTION

The sample of local tadpole galaxies selected in Paper I comes from the Kiso survey of UV intense galaxies (Miyauchi-Isobe et al. 2010). Among those galaxies labelled in the Kiso catalog as clumpy or having conspicuous HII regions, we visually inspected 158 with images in SDSS-DR7 (Abazajian et al. 2009). Then tadpoles were subjectively selected as those objects with lopsided light distribution, so that the brightest clump is far to one end and the rest of the galaxy is mostly featureless. This inspection rendered only 13 targets, which we completed with one additional galaxy with similar features from the University of Michigan survey of emission-line objects (MacAlpine & Lewis 1978). Half of the sample in Paper I was randomly selected for the follow-up work presented in this paper. The observing program was aimed at determining the dynamical properties of the galaxies based on long slit spectroscopic observations along the well-defined head-tail direction (see Fig. 1). The project was planned for the spectrograph IDS of the 2.5 m Isaac Newton Telescope (INT) at the Observatorio del Roque de Los Muchachos (Laing & Jones 1985). It provides adequate spectral resolution to determine centroids of emission lines with an accuracy better than 10 km s^{-1} , which suffices to characterize RCs even for dwarf galaxies. The original project could not be completed due to poor weather conditions, so it was finished using service time of the 2.5 m Nordic Optical Telescope (NOT), operated in the same observatory (Andersen 1985).

The observing logbook is summarized in Table 1. The used IDS@INT setup includes a grating with $1800 \text{ lines mm}^{-1}$, which provides a scale in the spectrograph focal plane of 0.32 Å pix^{-1} equivalent to $0''.44 \text{ pix}^{-1}$. The spectral resolution is set by the width of the $1''$ slit, which corresponds to 2.2 pix , or 0.73 Å , or 33 km s^{-1} in $H\alpha$. The camera covers some 700 Å around the central wavelength, which was tuned to $H\alpha$, and which automatically included the line $[\text{NII}]\lambda 6583$ used in our metallicity estimates (Sect. 3). The tadpoles KISO3193, KISO3867, KISO5149 and KISO8466 were observed with this setup (Table 1). Figure 2 shows one of them as an example. The image contains the spectral region around $H\alpha$. The reduction procedure included the standard bias and flatfield corrections, cosmic ray elimination, as well as removal of sky emission lines. The typical signal-to-noise (S/N) ratio in the peak $H\alpha$ emission exceeds 500, and it decreases down to one in the outskirts of the galaxy (Fig. 2, bottom panel). This S/N is achieved after integrating for some one and a half hours (Table 1). Seeing was of the order of $1''$ (Table 1).

The other three galaxies, KISO5639, KISO6669, and KISO6877 were observed with the NOT telescope with an observational setup equivalent to the previous one. We

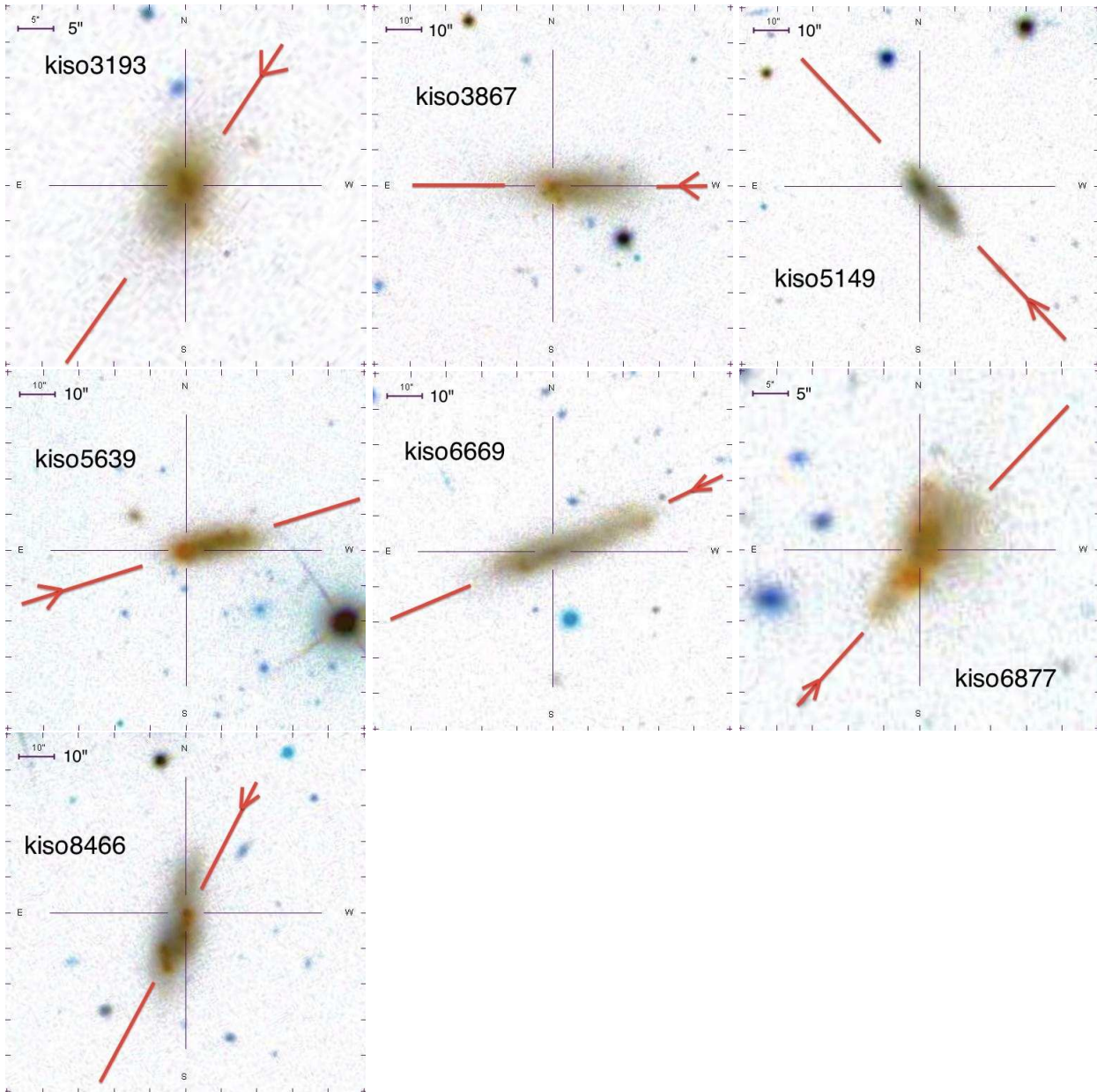


FIG. 1.— Images of the observed galaxies with the red line showing the orientation of the slit and with the arrow indicating the sense of increasing distance along the slit used in the paper. The images have been taken from the SDSS database, and are displayed with an inverted color palette so that the background sky looks white, and the intrinsically blue galaxies appear reddish. The horizontal scales on the upper left corner of the panels correspond to 5'' or 10'' as indicated.

used the ALFOSC spectrograph which, together with a high resolution grism, provided a scale of $0.26 \text{ \AA pix}^{-1} \times 0''.19 \text{ pix}^{-1}$ at $H\alpha$. This pixel size over-samples the spectrum, whose resolution was set by the $0''.9$ wide slit. In order to match the pixel size to the actual resolution, the original data were re-binned 2×2 , yielding the final resolution indicated in Table 1. The data reduction followed the standard process mentioned above, with a small difference worthwhile mentioning. The standard procedure includes using images of the sky taken during twilight to characterize (and then to correct for) large-scale illumination gradients in the images. Such sky-flat images corresponding to KISO6877 were not available. For reduction we used those from the previous night, but this rendered spectra with small residual sky lines.

To estimate the uncertainties introduced by this problem, the reduction was independently repeated by two of us (JSA and JMA). Thus different spectral regions and interpolations were used to construct the flatfield and to subtract the sky background. The two reductions are in good agreement and provide consistent results. Table 2 contains the final physical parameters inferred from the two parallel reductions, and they agree to the point that their small differences do not affect the results in the work. Seeing during observations was sub-arcsec. The NOT spectra have S/N similar to the INT spectra; the spectral resolution is slightly worse, and the angular resolution slightly better.

Determining the actual spectral resolution is central for the proper interpretation of the observed linewidths.

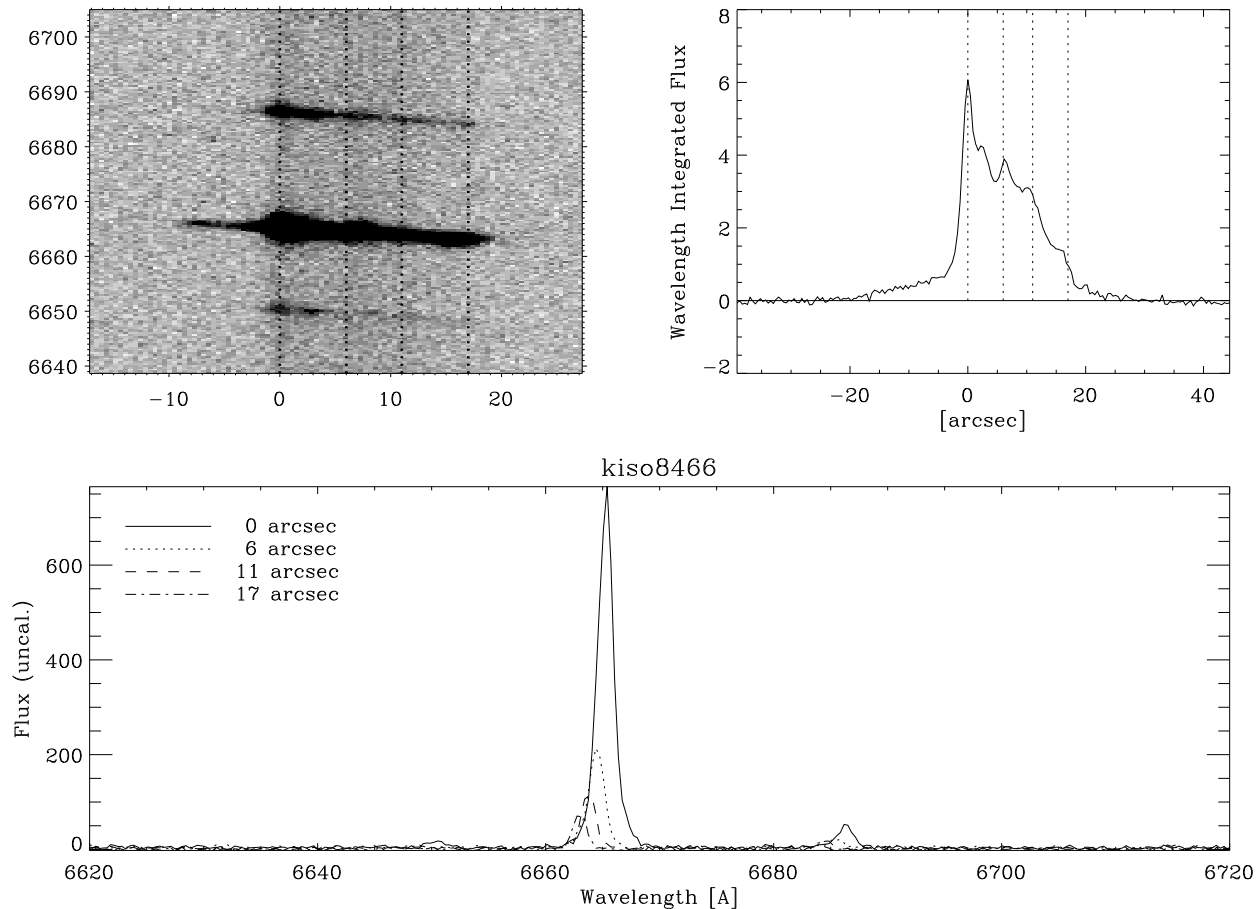


FIG. 2.— Example of a reduced spectrum from IDS@INT. The image shows a negative of the spectrum after reduction – x-axis represents position and y-axis wavelength. Positions are given in arcsec from the galaxy head, whereas wavelengths are in Å. The wavelength integrated flux (spectral flux) is shown in the top right corner. Spectra corresponding to various positions are shown in the bottom panel, with the positions indicated as vertical dotted lines in the two upper plots. The example corresponds to KISO5149, but it is representative of the full set. The largest line is H α whereas the second largest is [NII] λ 6583, used in our metallicity estimates.

As usual, it was determined from the width of the telluric lines in the spectra since their intrinsic widths are just a few km s^{-1} and thus negligible (e.g., Balthasar et al. 1982). Gaussian functions were fitted to the lines, and their mean Full Width Half Maximum (FWHM) are quoted in Table 1 as the spectral resolution, with the error bars representing the rms fluctuations along the field of view. We average over all the targets observed with the same instrumental configuration to estimate the resolution corresponding to that particular configuration. The weighted average for the IDS@INT spectra turns out to be $25.4 \pm 0.6 \text{ km s}^{-1}$, whereas in the case of ALFOSC@NOT the measured resolution is $54.4 \pm 3.9 \text{ km s}^{-1}$. The error bars represent the weighted rms fluctuations.

3. DETERMINATION OF PHYSICAL PARAMETERS

Velocities, masses, abundances and other physical parameters are determined from the spectra. This section explains how these parameters are computed, including the underlying hypotheses and their uncertainties.

Bulk velocities are measured from the displacement of H α . We compute the displacement both as the barycen-

ter of the emission line, and as the center of a Gaussian function fitted to the profile. Errors are estimated from the S/N measured in the continuum and then propagated to the centroids (e.g., Martin 1971, Sect. 5.3). The FWHM of the profiles are also measured directly from the profile and from the Gaussian fit. Their errors are also inferred from the noise measured in the continuum by error propagation.

The variation of the velocity with position along the slit is usually referred to as the velocity curve. The velocity curves of our targets can be ascribed to rotation. In order to characterize such rotation, we fit an analytic RC to the velocity curve. We wanted a function that is simple but produces a good match to the observations. The *universal* RC advocated by Salucci et al. (2007) does a good job representing the observed variation. Specifically, we adopted the dark matter component of the universal RC given by,

$$U(d) = U_0 + U_1 \frac{d - d_0}{\sqrt{\Delta^2 + (d - d_0)^2}}, \quad (1)$$

where $U(d)$ is the velocity observed at a distance d , and U_0, U_1, Δ , and d_0 are free parameters to be determined from a non-linear fit. The curve is simple – d_0 yields a

TABLE 1
OBSERVING LOGBOOK

Name ^a	RA	DEC	t_{exp}^b [s]	Date 2012	Instrument	Slit	Seeing ^c	Pixel	Scale [pc/'']	Telluric ^d [km s ⁻¹]
KISO3193	08:56:08	+39:52:09	6000	Feb 10	IDS@INT	1''0	1''0	0.32Å×0'44	124	26.0±1.9
KISO3867	09:40:13	+29:35:30	6000	Feb 10	IDS@INT	1''0	1''0	0.32Å×0'44	36	25.0±1.0
KISO5149	11:16:08	+23:29:16	6000	Feb 10	IDS@INT	1''0	1''0	0.32Å×0'44	834	28.2±1.5
KISO5639	11:41:07	+32:25:37	5000	May 29	ALFOSC@NOT	0''9	0''8	0.51Å×0'38	119	53.9±5.7
KISO6669	12:31:50	+27:23:13	5000	May 29	ALFOSC@NOT	0''9	0''8	0.51Å×0'38	299	55.6±8.7
KISO6877	12:46:11	+26:15:01	5000	May 31	ALFOSC@NOT	0''9	0''7	0.51Å×0'38	128	54.3±6.6
KISO8466	16:03:27	+19:09:46	4800	Feb 10	IDS@INT	1''0	1''0	0.32Å×0'44	313	24.9±0.7

^a Named as in Elmegreen et al. (2012b), Paper I.

^b Total exposure time.

^c Mean value for the night from RoboDIMM@WHT; see <http://catserver.ing.iac.es/robodimm/>.

^d FWHM of the observed telluric lines, used as proxy for spectral resolution.

center for the RC, U_1 gives its amplitude ($U \rightarrow U_0 \pm U_1$ when $d \rightarrow \pm\infty$), and Δ provides the spatial scale for the central gradient. We stress that the hypotheses behind the analytic expression (1) are of little importance in our context. The formula is used here because it provides a good representation of the observations, and so provides a smoothed version of the velocity curve. Moreover, it allows us to determine the center of rotation d_0 . The center thus determined does not depend so much on the actual expression used to parameterize the RC, but on the fact that the curvature changes sign at the center of rotation, i.e.,

$$U''(d_0) = 0, \quad (2)$$

with U'' the second derivative of U . This is a general property that any anti-symmetric RC satisfies.

Dynamical masses are estimated from RCs and linewidths. Assuming the mass distribution to be spherically symmetric (e.g., a bulge or a dark matter halo), the circular velocity U_c that balances the gravitational pull depends only on the mass enclosed within the radius ρ , $M(\rho)$,

$$U_c^2(\rho) = G M(\rho)/\rho, \quad (3)$$

with G the gravitational constant. We assume that the measured macroscopic velocities are the circular velocities affected by the inclination i of the galaxy plane, i.e., $U = U_c \sin i$. We also assume the spectrograph slit to be oriented along the galaxy major axis, implying $\rho = d - d_0$. Then the inner mass of the galaxy up to distance d has the usual expression,

$$M(d) \sin^2 i = (d - d_0) U^2(d)/G, \quad (4)$$

which using astrophysical units turns out to be

$$M(d) \sin^2 i = (2.33 \cdot 10^5 M_\odot) (d - d_0) U(d)^2, \quad (5)$$

with d measured in kpc and U in km s⁻¹. Equation (5) is an approximation; however, including more realism in the mass distribution (e.g., pressure support, Dalcanton & Stilp 2010; or non-spherical components, Salucci & Persic 1997) would only modify the scaling factor as a correction of order one. Masses of individual clumps are inferred from linewidths assuming virial equilibrium. If the isotropic velocity distribution that balances the clump gravity has a dispersion σ , then

(Bosch et al. 2009, Sect. 4.2)

$$M = (1.20 \cdot 10^5 M_\odot) R_e \text{FWHM}^2, \quad (6)$$

where

$$\text{FWHM} = 2\sqrt{2 \ln 2} \sigma. \quad (7)$$

The symbol R_e stands for the half-light radius of the clump, so that Eq. (6) is equivalent to Eq. (5) after including the appropriate scaling factors. As in the case of Eq. (5), distances are measured in kpc and linewidths in km s⁻¹. The linewidth in Eq. (6) is not the observed width FWHM_o , but the width corrected for instrumental spectral resolution FWHM_i , thermal motions in the nebula FWHM_t , and natural width of H α FWHM_n ,

$$\text{FWHM}^2 = \text{FWHM}_o^2 - \text{FWHM}_i^2 - \text{FWHM}_n^2 - \text{FWHM}_t^2, \quad (8)$$

see, e.g., Terlevich & Melnick (1981); Melnick et al. (1999). We use the measured widths of the telluric lines as proxy for instrumental broadening (Table 1). The thermal broadening is assumed be the same for all galaxies at all positions. Its value has been set to a representative round number $\text{FWHM}_t = 25 \text{ km s}^{-1}$, which approximately corresponds to H atoms at 14000 K, a temperature typical of HII regions. The actual FWHM_t is of secondary importance since the range of possible values is significantly smaller than the FWHM resulting from Eq. (8)⁵. Finally, the natural width of H α is of the order of 7 km s^{-1} (e.g., Rozas et al. 2006). The radius R_e used to estimate dynamical masses from line widths using Eq. (6) is computed fitting a 1-D Gaussian to the light distribution across the galaxy head. The observed light profile is assumed to represent a 1-D cut across the center of a 2D-Gaussian, which readily provides the half-light radius from the width of the fitted Gaussian – in a 2D Gaussian, the FWHM is twice the half-light radius. The observed radii are corrected for seeing using a formula

⁵ FWHM_t varies only from 19 to and 26 km s⁻¹ for temperatures between 8000 and 15000 K. Moreover, we did the exercise of calculating masses also with the extreme value of $\text{FWHM}_t=0$, to check that this assumption does not modify the conclusions in the work. Setting $\text{FWHM}_t=0$ is equivalent to including thermal motions as part of the virial equilibrium represented by Eq. (6). The exercise implies that we do not have to worry about whether the thermal motions contribute or not to the virial equilibrium. Including or not thermal motions as part of the kinetic energy does not significantly modify the masses estimated in the work.

similar to Eq. (8), namely,

$$R_e^2 = R_{e0}^2 - (S/2)^2, \quad (9)$$

where R_{e0} stands the measured effective radius and S represents the seeing, i.e., the FWHM of the seeing disk as given in Table 1.

The metallicity of the gas is commonly inferred by combining emission-line fluxes of several atomic species to derive their relative abundances (e.g., Pagel & Edmunds 1981; Osterbrock 1989). This approach is the so-called direct method or temperature-based method, and it is to be preferred whenever possible. However, it involves measuring fluxes of lines spread throughout the visible-IR spectrum, so is expensive observationally. Fortunately, we have alternatives called strong-line methods (e.g., Shi et al. 2005; Kewley & Ellison 2008), where the metallicity is estimated empirically by relating the ratio of a few selected line fluxes with the abundance of a particularly relevant metal (typically oxygen). The one proposed by Denicoló et al. (2002) turns out to be ideal in our case, when only the spectral region around $H\alpha$ is available. It yields the oxygen abundance from the ratio of $[NII]\lambda 6583$ to $H\alpha$, and $[NII]\lambda 6583$ automatically appears in the spectra next to $H\alpha$ (see Fig. 2). We use the calibration by Pérez-Montero & Contini (2009),

$$12 + \log(O/H) = 9.07 + 0.79 \log([NII]\lambda 6583/H\alpha), \quad (10)$$

particularly suited for low metallicity targets (c.f., Pettini & Pagel 2004). Equation (10) provides the O metallicity from the flux in a N line, therefore, it may be biased in objects having unusual N/O. In order to discard this potential bias in our O metallicities, we also estimate the ratio of N to O using the sulfur lines $[SII]\lambda 6717$ and $[SII]\lambda 6731$ present in most of our spectra. We use the calibration

$$\log(N/O) = 1.26 \log([NII]\lambda 6583/[SII]\lambda 6717, 6731) - 0.86, \quad (11)$$

also by Pérez-Montero & Contini (2009).

The *spectral flux* of the galaxy is computed by integrating the observed spectra between their two extreme wavelengths (from 6242 Å to 6935 Å for INT spectra, and from 6368 Å to 6840 Å for NOT spectra). The flux in $H\alpha$ results from integration of the emission line profile around its maximum, once the underlying continuum was removed. The integration includes a 10 Å wide region around the peak emission, whereas the continuum was obtained by fitting a linear function to two continuum windows, 10 Å wide, outside the line. The $H\alpha$ equivalent width (EW) is inferred from the $H\alpha$ flux dividing by this continuum. Continuum and emission lines are combined in the *spectral flux* for simplicity, and it suffices to compare the limited extension of the emission line region inferred from $H\alpha$ with the rest of the galaxy.

4. VELOCITY CURVES AND LINEWIDTHS

Figure 3 shows the velocity curves of the tadpole galaxies included in our study. Five out of the seven targets show velocity gradients interpreted as rotation. The figure includes the best fit to the analytic RC in Eq. (1), which does a good job reproducing the observations. We use for fitting the portion of the velocity curve indicated in red in Fig. 3, which includes all positions but the

extremes with large error bars or obvious distortions. Sometimes the interpretation of the velocity curve as a RC is obvious (e.g., KISO8466), but other times the curve looks more like a perturbed RC (e.g., KISO5639). KISO3193 and KISO3867 have a rather flat velocity curve, and therefore no obvious rotation. However, one of them, KISO3867, shows a systematic line shift of the order 10–20 km s^{−1} between the two extremes of the galaxy (Fig. 3). The amplitude is of the order of the error bars, but the displacement is in the raw data as judged by inspection of the individual $H\alpha$ profiles. Table 2 contains the amplitudes of the RCs as assigned by the fit (i.e., U_1 in Eq. [1]). Figure 3 represents velocities obtained from the barycenter of $H\alpha$ (Sect. 3). The velocities from the Gaussian fit are not shown because the two estimates differ only by a few km s^{−1}, a difference always smaller than the error bar assigned to each velocity measurement.

Table 2 also contains the center of rotation d_0 , which often differs from zero, i.e., from the position of the tadpole head. As argued in Sect. 3, its estimate is fairly robust since it comes from the point where the curvature of the RC changes sign – accordingly, it has the small formal error bars provided in Table 2. Figure 3 shows that three out of the five rotating galaxies, explicitly KISO6669, KISO6877 and KISO8466, have their center of rotation displaced with respect to the head by more than the 1'' uncertainty introduced by seeing (see Table 1). Considering that the rotation center points out the center of the galaxy, our results indicate that often the star-forming region at the head is displaced with respect to the center of the galaxy. This suggests that the head is not a bulge-like central spheroid. The fact that the center of rotation is sometimes displaced from the heads may be easier to appreciate in Fig. 4.

Figure 5 shows the FWHM of $H\alpha$ as inferred directly from the emission line profile (the solid lines) and from the Gaussian fit (the dashed lines). A significant part of the observed linewidths is due to instrumental broadening. The widths corrected for instrumental effects and thermal motions are given as dotted lines in the figure. We use the directly inferred widths to estimate the intrinsic widths, but using them or the widths from the Gaussian fit render similar results since the two measurements are in very good agreement (Fig. 5). First note that the widths of all galaxies, large and small, are of the order of 20–70 km s^{−1}. These widths are typical of giant HII regions such as 30 Doradus rather than the widths of the HII regions observed in large spirals (e.g., O'dell & Townsley 1988; Muñoz-Tuñón 1994). Figure 6 shows the variation of the tadpole head size as a function of its velocity dispersion. The two quantities are known to be correlated in giant HII regions, so that the larger the dispersion the larger the size (e.g., Muñoz-Tuñón 1994; Fuentes-Masip et al. 2000). We find the tadpole heads to follow such trend as characterized by Terlevich & Melnick (1981), Roy et al. (1986), or more recently by Wisnioski et al. (2012) (see Fig. 6). In the case of KISO6877, the error bars of the line width at the head are so large that the width is actually an upper limit, but even with this caveat in mind, the measurement is consistent with its head being a giant HII region (Fig. 6).

The FWHM also varies along the galaxies, and the fluctuations are correlated neither with the spectral flux

TABLE 2
PHYSICAL PARAMETERS

Name ^a	Distance ^a [Mpc]	FWHM ^b [km s ⁻¹]	log M_h D ^c [M_\odot]	R_e ^d [kpc]	log M_h Ph ^e [M_\odot]	U_1 ^f [km s ⁻¹]	d_0 ^g [kpc]	log M D ^h [M_\odot]	log M Ph ⁱ [M_\odot]	12+log(O/H) ^j
KISO3193	25.5	39.3 ± 2.0	7.61 ± 0.04	0.221 ± 0.009	6.4 ± 0.1	7.3 ± 0.4	7.89 ± 0.31
KISO3867	7.4	35.4 ± 2.2	7.22 ± 0.04	0.109 ± 0.003	5.2 ± 0.3	6.8 ± 0.4	8.03 ± 0.26
KISO5149	172	70.1 ± 3.0	9.03 ± 0.03	1.825 ± 0.064	8.9 ± 0.1	168 ± 92	0.3 ± 3.0	10.8 ± 0.6	9.6 ± 0.4	8.42 ± 0.06
KISO5639	24.5	46 ± 11	7.22 ± 0.15	0.065 ± 0.004	6.7 ± 0.2	34.7 ± 6.2	0.180 ± 0.064	8.2 ± 0.2	7.7 ± 0.4	7.48 ± 0.04
KISO6669	61.6	47 ± 11	7.73 ± 0.14	0.206 ± 0.011	7.0 ± 0.1	71.4 ± 4.6	1.24 ± 0.16	9.8 ± 0.1	8.9 ± 0.4	8.11 ± 0.12
KISO6877	26.3	22 ± 23	6.19 ± 0.66	0.028 ± 0.004	6.3 ± 0.1	19.0 ± 1.7	0.246 ± 0.020	7.7 ± 0.1	7.3 ± 0.4	7.40 ± 0.09
KISO6877 ^k	26.3	21 ± 24	6.30 ± 0.70	0.038 ± 0.003	6.3 ± 0.1	19.0 ± 1.6	0.242 ± 0.020	7.6 ± 0.1	7.3 ± 0.4	7.41 ± 0.07
KISO8466	64.5	61.0 ± 2.9	8.19 ± 0.04	0.345 ± 0.021	8.1 ± 0.1	117 ± 16	2.95 ± 0.36	10.0 ± 0.1	9.2 ± 0.3	8.14 ± 0.05

^a From Elmegreen et al. (2012b), Paper I.

^b H α width at the tadpole head.

^c Dynamical mass of the head – from Eq. (6).

^d Half-light radius of the head.

^e Photometric mass of the head, from Paper I, Table 3.

^f Amplitude of the rotation curve – see Eq. (1).

^g Center of rotation relative to the tadpole head – see Eq. (1).

^h Dynamical mass of the galaxy – see text for its computation.

ⁱ Photometric mass of the galaxy, from Paper I, Table 3.

^j Metallicity at the head – from Eq. (10).

^k Second independent reduction.

nor with the H α flux (c.f. Fig. 4 and 5). If anything, there is a tendency for the tadpole heads to coincide with local minima of linewidth (see KISO5149, KISO5639, and KISO6877 in Fig. 5). Similarly, the center of rotation of the rotating galaxies does not seem to be associated with extremes of the FWHM curve. Interpreting the decrease of linewidth associated with the head is not straightforward. One may try to explain its origin in the context of forming stars in a highly turbulent galaxy. Only where the turbulence is low enough the conditions that trigger star formation are met, and this preference for low turbulence regions is what we detect.

The square of the ratio between velocity dispersion and rotation gives the Jeans length relative to the galaxy size (e.g., Bournaud & Elmegreen 2009). In other words, it provides the relative size of the clumps to be produced by gravitational instability. Using Eq. (7) and the data in Table 2, the ratio dispersion to rotation σ/U_1 turns out to be between 0.2 and 0.6 at the tadpole heads, which yields expected clump sizes between 0.03 % and 30 % galaxy radii. The relative size increases with decreasing galaxy mass, and it may be a coincidence, but the largest ratios correspond to the two XMP galaxies in the sample (see Sect. 7). In some cases the predicted clumps have sizes comparable to those of the observed heads. The ratio σ/U_1 also measures whether the object is supported by random motions or rotation. Our disks have ratios similar to the turbulence-supported clumpy galaxies observed at high redshift (e.g., Ceverino et al. 2012).

5. FLUXES AND EQUIVALENT WIDTHS

Figure 4 shows the variation across the galaxies of the spectral flux and the H α flux (the solid lines and the dashed lines, respectively). The position where the two fluxes are largest coincides. (As we already pointed out, the origin of distances used along the paper has been set at the maximum of the spectral flux distribution.) Note also the obvious lopsidedness of all light curves, as expected in tadpole galaxies. Another important feature is the extension of the H α emission as compared to

the spectral flux emission which includes H α plus continuum. H α is more concentrated, implying that the region producing the total emission extends further away from the star-forming regions. In other words, it shows the existence of an underlying galaxy, with old stellar populations that contribute to the spectral flux but not to H α .

The dotted line in Fig. 4 represents a Gaussian plus a constant term fitted to the H α flux around the head. The fits are good, and they allow us to assign a radius to the head. Table 2 lists the effective radii of the heads R_e , defined as the radius enclosing half of their light (see Sect. 3). They span a wide range of values from 1.8 kpc to 50 pc, reflecting the wide range of intrinsic galaxy sizes.

Figure 7 shows the variation of H α EWs across the galaxies. The largest EWs tend to coincide with the maximum flux (Fig. 4), although not always (KISO3193 in Fig. 7). In general, EWs are fairly moderate, with maxima $\lesssim 300$ Å. The two exceptions correspond to the two extremely metal poor targets to be described in Sect. 7 – KISO5639 and KISO6877. Their large H α EW implies the extreme youth of the star-forming regions at the galaxy head. We know from modeling that the H α EW of an HII region must be smaller than some 3000 Å, and it drops down very quickly so that a coeval starburst reaches EW $\simeq 200$ Å in just 10 Myr (e.g., Leitherer et al. 1999, Fig. 83). There is also a dependence of the EW on metallicity, but age is by far the dominant factor. The large observed H α EWs correspond to ages of only a few Myr, and these ages are upper limits to the stars responsible for the ionization since the (old) underlying galaxy produces continuum emission that reduces the observed EW. If KISO5639 and KISO6877 are as young as we infer from their H α EWs, one expects to find Wolf-Rayet (WR) star features in the spectra, which are characteristics of extremely young starbursts (< 5 Myr; e.g., Crowther 2007). These features are distinctive broad bumps at 4600–4680 Å and 5650–5800 Å (e.g., Schaerer et al. 1999; Brinchmann et al. 2008). Unfortunately, the WR features lie outside our observed spectral range. However,

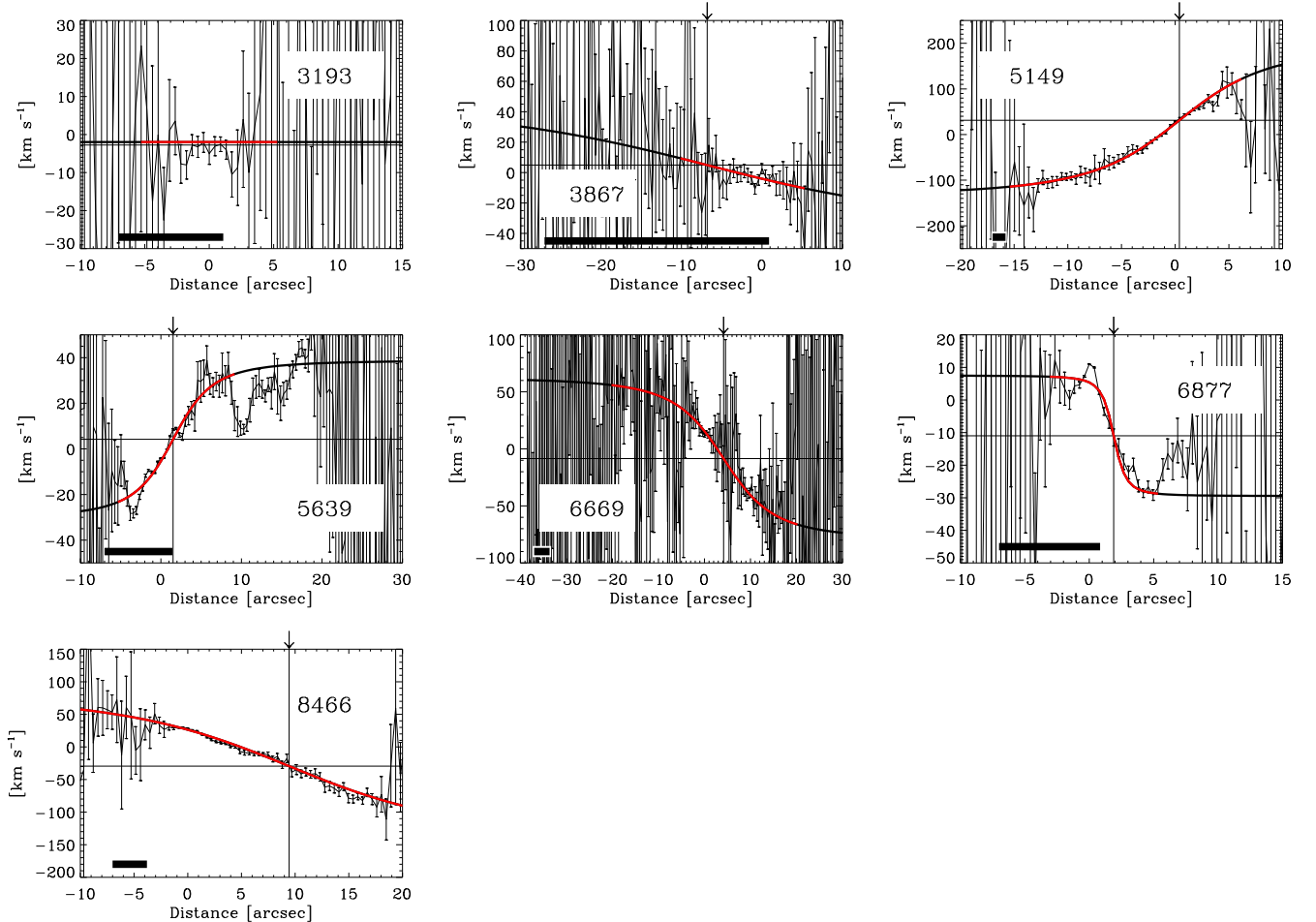


FIG. 3.— Velocity curves of the seven tadpole galaxies. The abscissae represent distances along the major axes of the galaxies from the position of the tadpole head; i.e., the brightest point on the galaxy. The range of distances differs for the different targets, but the horizontal bar in each panel gives a common length scale corresponding to 1 kpc. The points with error bars show the observations whereas the thick solid line represents the best fit of the observed points to the analytic RC. The part of the RC shown in red indicates the portion of the velocity curve used for fitting. The thin horizontal and vertical lines indicate the systemic velocity and the center of rotation obtained from the fit, respectively. The little arrows on top of each panel also indicates the center of rotation. The zero of the velocity scale is set by velocity of the spatially integrated spectrum of the galaxy. Positive velocities are redshifts. The ordering of the galaxies is identical to that in Fig. 1.

our galaxies also have SDSS spectra, which cover a wider range (Stoughton et al. 2002; Abazajian et al. 2009). We inspected them for WR features but we did not see any (see Fig. 8). Moreover, our targets were not found in the systematic search for WR galaxies in SDSS carried out by Brinchmann et al. (2008). KISO6877 does not show WR features, most probably because the SDSS spectrum was taken away from the tadpole head, in a region which is not particularly young. KISO5639 does not show the broad WR features either. Instead, its spectrum contains narrow high excitation emission lines including HeII λ 4686 (Fig. 8). These lines are supposed to be excited only by the hard UV-radiation of WR stars, which makes interpreting spectra with HeII λ 4686 but without WR bumps puzzling (see, Shirazi & Brinchmann 2012). However, there is a significant number of star-forming galaxies without WR features showing HeII λ 4686 emission. The reason is unknown, but these galaxies are usually metal-poor (Shirazi & Brinchmann 2012), so that the presence of high excitation narrow lines seems to reflect the extreme youth of a metal-poor starburst. Ac-

cording to Shirazi & Brinchmann (2012), the stellar populations at very low metallicities can have much higher temperatures than is currently expected in models. Then even main sequence O stars may excite HeII λ 4686. Alternatively, in low metallicity environments the winds of WR stars are weak, and so, optically thin in the He+ continuum, allowing the ionizing radiation to escape creating an HeIII region responsible for the observed emission (see Kehrig et al. 2011, and references therein). In short, even though KISO5639 lacks WR bumps, the presence of high excitation lines such as HeII λ 4686 reinforces our conclusion that its head contains an extremely young metal-poor starburst.

6. DYNAMICAL MASSES

Figure 9 shows the relationship between the dynamical mass and the photometric mass for the tadpole heads and the full galaxies. The photometric masses are from Paper I, whereas the dynamical masses come from applying Eqs. (5) and (6). In particular, Eq. (5) has been integrated until the last point used to compute the RC. The

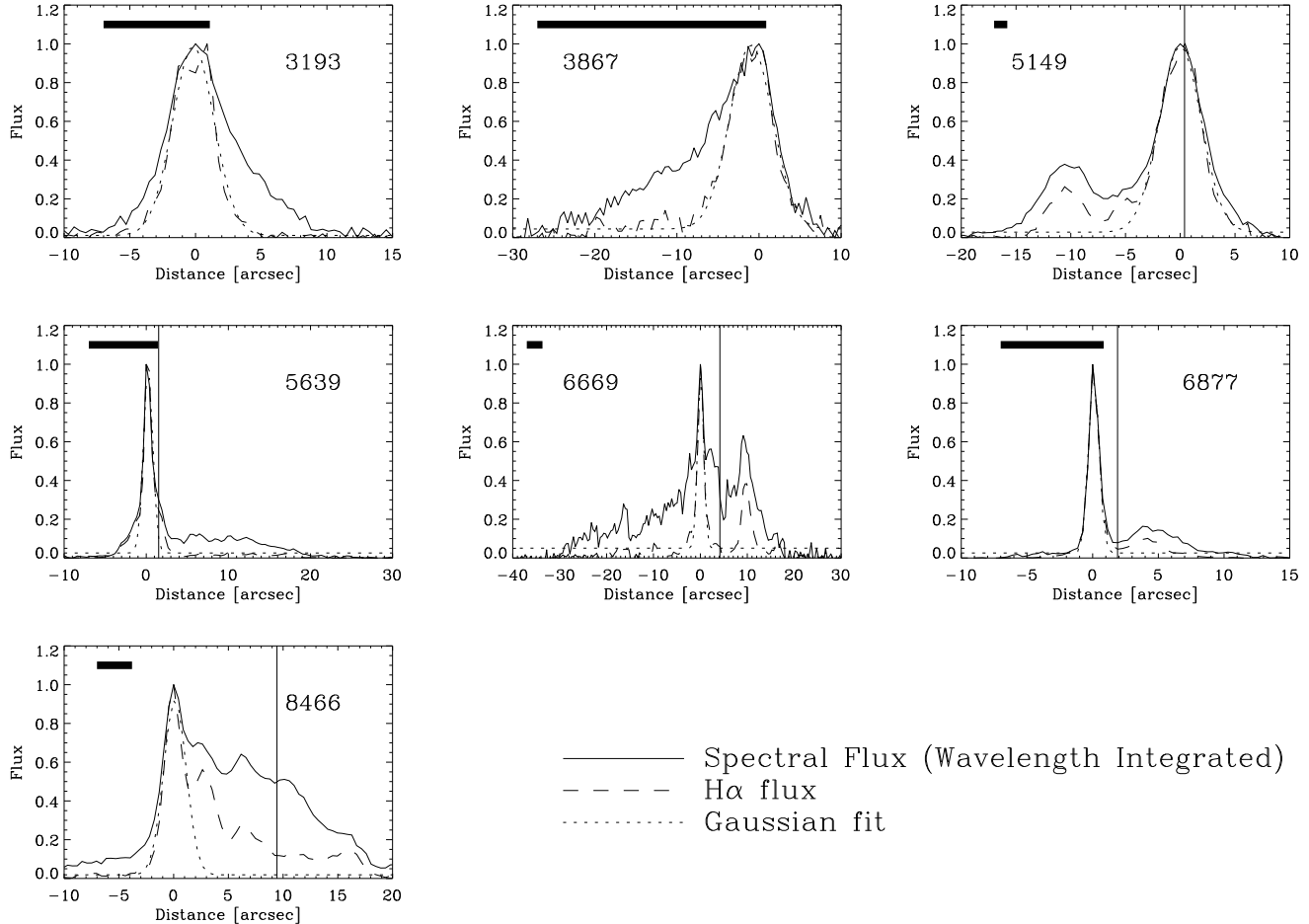


FIG. 4.— Spectral flux (the solid lines) and $H\alpha$ flux (the dashed lines). Note the obvious lopsidedness of the light distributions, as expected in tadpole galaxies. The origin of distances has been set as the maximum of the spectral flux distribution. The dotted line represents a Gaussian fitted to the $H\alpha$ flux around the head. The horizontal bar in each panel gives a common length scale corresponding to 1 kpc. Formal error bars for photometry are not included since they are negligible small. The thin vertical solid lines indicate the center of rotation obtained from the RC fit shown in Fig. 3. The ordering of the galaxies and the range of abscissae are identical to those in Fig. 3.

actual values used for plotting are listed in Table 2. Note that all dynamical masses are larger than the photometric masses. The difference is less important in the heads (except for the case of KISO3867, discussed in Sect. 8). Three of the heads have almost identical dynamical and photometric masses, so in these cases there appears to be no dark matter in the heads (KISO5149, KISO6877, and KISO8466). Keep in mind that the dynamical masses of the galaxies derived from RCs are actually lower limits. First, there is a $\sin^2 i$ factor in Eq. (5). It is probably unimportant since our galaxies are elongated suggesting large inclinations and so $\sin^2 i \sim 1$. Second, and more critical, is the fact that the RC has been integrated only to the largest radii having velocities. Since the dynamical mass of the galaxies thus derived exceeds the photometric mass, we can conclude that galaxies are objects with significant amounts of non-stellar matter.

If the star-forming regions at the head of the tadpole were self-gravitating, one would expect them to hold some degree of internal rotation. If this rotation significantly differs from the galaxy rotation pattern, and if the head is massive enough, then the rotation of the head could perturb the rotation curve of the galaxy pro-

ducing a noticeable distortion (e.g., Immeli et al. 2004). We examined the observed RCs for such signals and did not find them, except perhaps in the case of KISO6877, discussed in Sect. 8.

7. METALLICITIES

The metallicity was estimated as explained in Sect. 3, using the ratio $[\text{NII}]\lambda 6583$ to $H\alpha$. Figure 10 shows the variation across the galaxies of the oxygen abundance, including their error bars. (Points with errors larger than 1 dex have been excluded.) The galaxies tend to have sub-solar metallicity (the thick horizontal line marks the solar oxygen abundance given by Asplund et al. 2009, $12 + \log(\text{O}/\text{H})_{\odot} = 8.69 \pm 0.05$). The galaxies also present significant abundance gradients, with the lowest abundances tending to coincide with the largest $H\alpha$ emissions (e.g., KISO6669 and KISO6877 in Fig. 10, keeping in mind that the vertical dotted lines mark the position of the peak $H\alpha$ fluxes). We also note that two targets, KISO5639 and KISO6877, have metallicities well below one-tenth the solar value, therefore, they belong to the selected club of XMP galaxies (e.g., Kunth & Östlin 2000; Guseva et al. 2003). They are really rare objects:

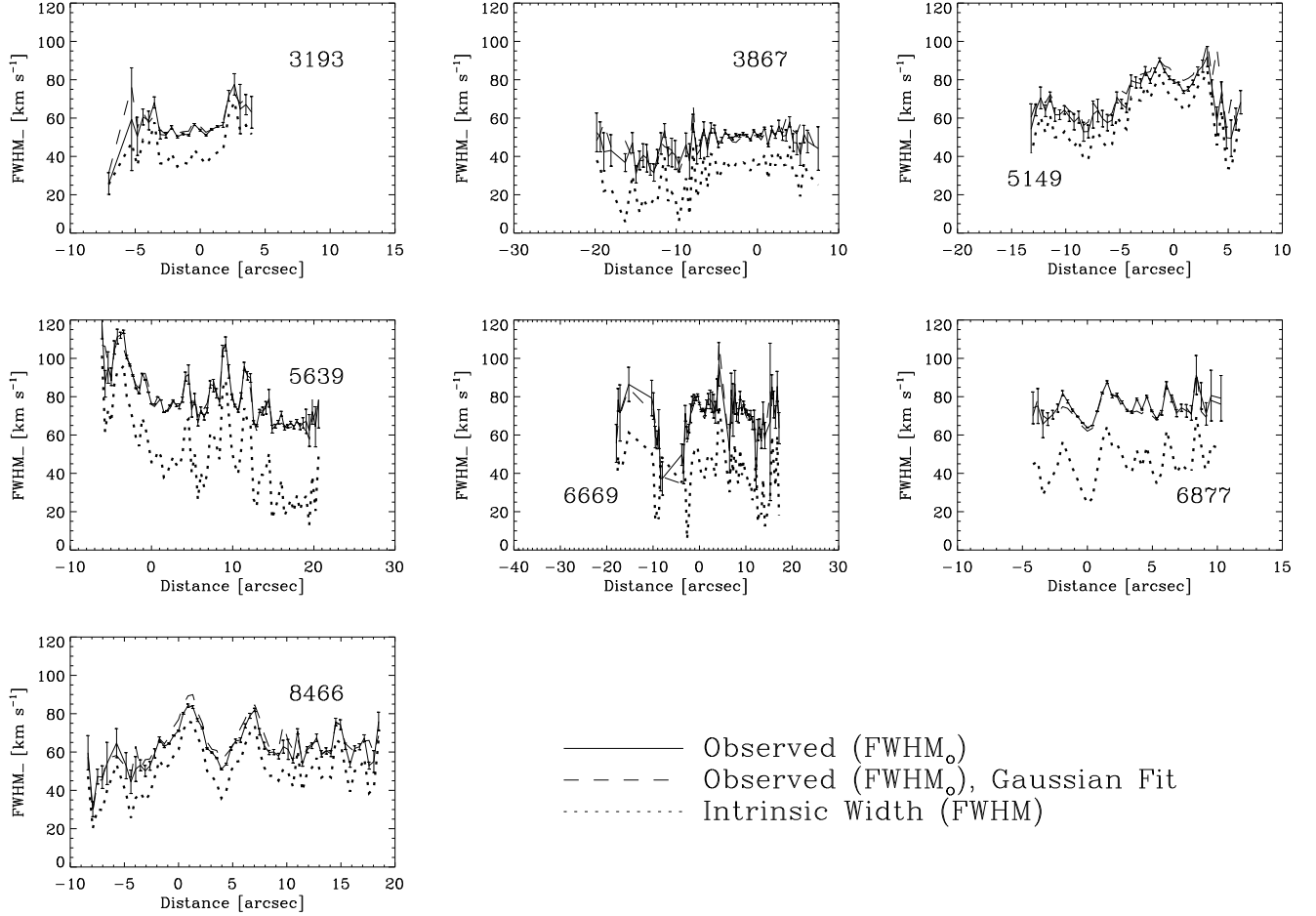


FIG. 5.— FWHM of $H\alpha$ inferred directly from the emission line profile (the solid lines), from the Gaussian fit (the dashed lines), and after correction for instrumental, thermal and natural broadenings (the dotted lines). Formal error bars for the direct measurement are represented too. The ordering of the panels and the abscissae are identical to those in Fig. 3.

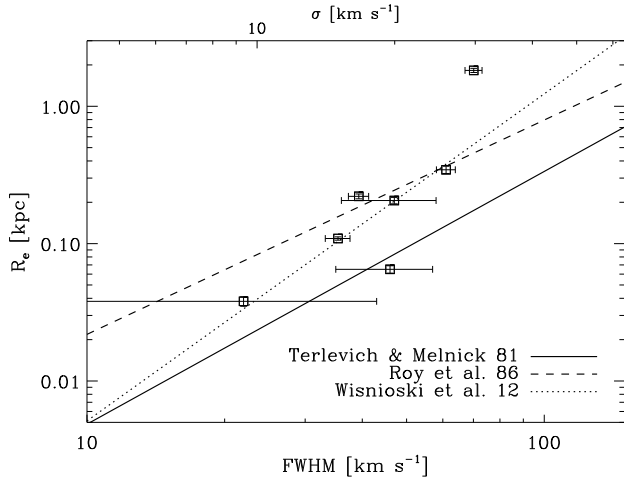


FIG. 6.— Half-light radius of the tadpole head versus $H\alpha$ linewidth. The velocity dispersions are usually parameterized in terms of $\sigma = \text{FWHM}/(2\sqrt{2\ln 2})$, and its scale is given in the abscissae on top of the figure. The observed points follow the trends observed in giant HII regions – solid, dashed, and the dotted lines correspond to the empirical calibration of the relationship by Terlevich & Melnick (1981), Roy et al. (1986), and Wisnioski et al. (2012), respectively.

one out of a thousand galaxies in the local universe according to Morales-Luis et al. (2011). Therefore the fact that we observe two in a sample of seven cannot be a coincidence. It is known that a significant fraction of XMP galaxies turn out to be cometary or tadpole (Papaderos et al. 2008; Morales-Luis et al. 2011). Here we find that the reverse holds too, i.e., that tadpole galaxies have a significant probability of being XMP. As we discuss in Sect. 9, this fact supports the idea that the tadpole morphology is a sign of dynamical youth, as the low metallicity is a sign of being chemically young.

The observed gradients in metallicity are one of the central results of this work and, therefore, deserve a separate discussion. Our abundance determinations are based on $N2=[\text{NII}]\lambda 6583/H\alpha$ rather than on the direct method, and this may be a source of systematic error (e.g., Shi et al. 2005). The spatial gradients in metallicity may be artificially due to gradients in excitation. As Morales-Luis et al. (2013, in preparation) discuss, the excitation and (to a lesser extent) N/O change $N2$ at $12 + \log(\text{O}/\text{H}) \simeq 7.5$. The higher the excitation the smaller $N2$, and the excitation is expected to change with time since the number of ionizing photons drops down quickly in young starbursts (e.g., Leitherer et al. 1999, Fig. 77). However, the bias the excitation pro-

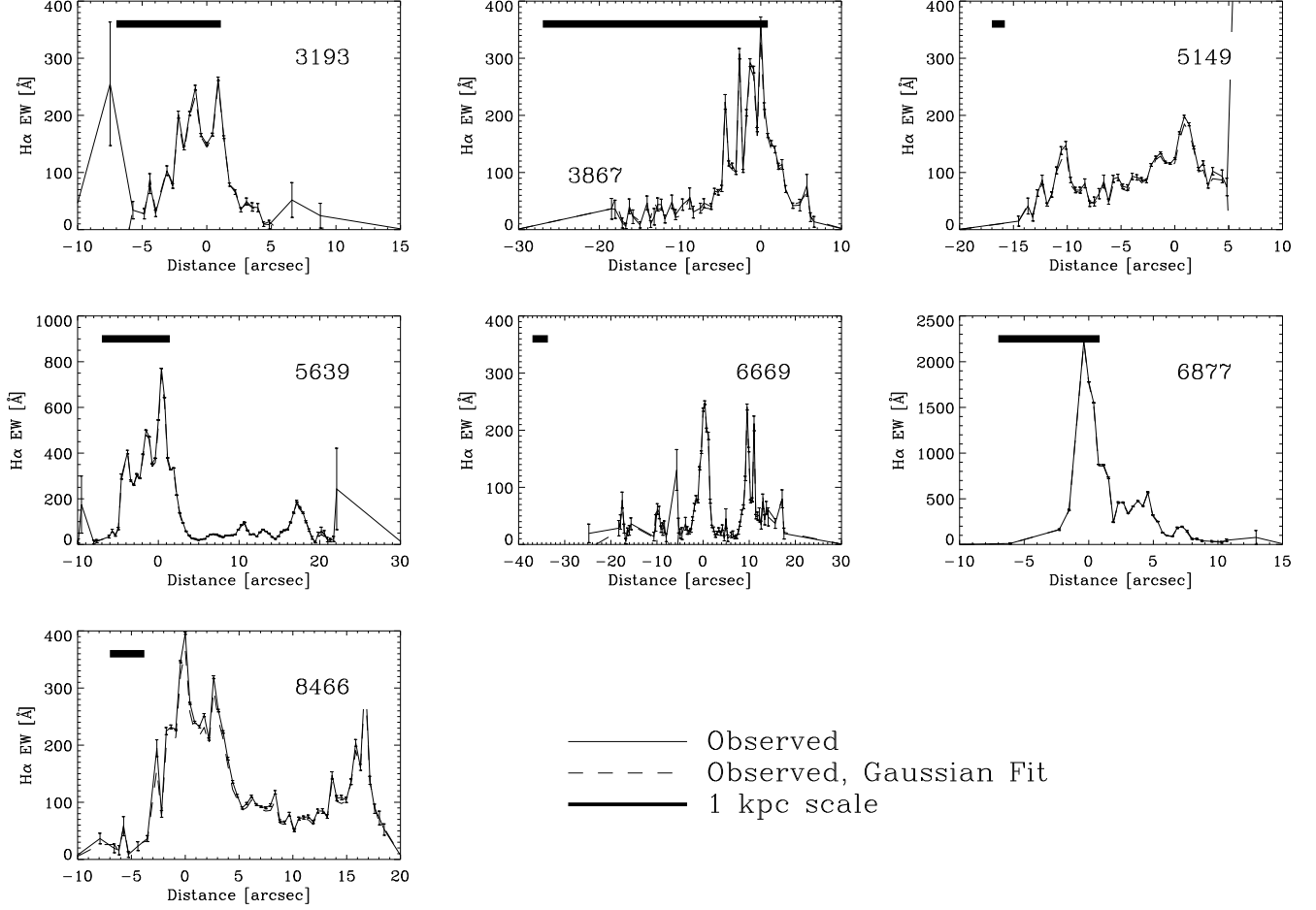


FIG. 7.— H α EW in \AA . EWs obtained directly from the line profile (the solid lines) and through a Gaussian fit (the dashed lines) are included, although they are difficult to distinguish. The range of distances differs for the different targets, but the horizontal bar in each panel gives a common length scale corresponding to 1 kpc. Only points where the EW is larger than its formal error bar are included. The ordering of the galaxies and the abscissae are identical to those in Fig. 3.

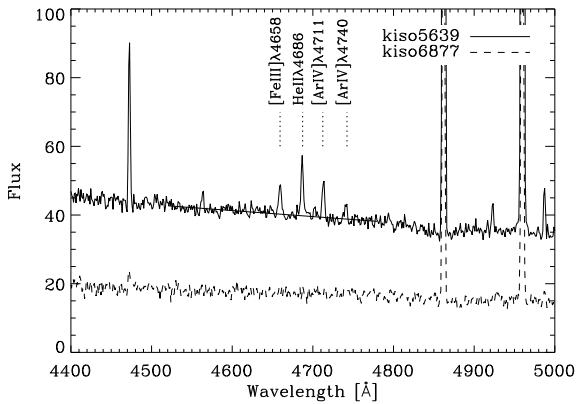


FIG. 8.— SDSS spectra of our two youngest targets in the wavelength region around one of the WR bumps (4600–4680 \AA). The bump is missing, but one of the targets shows a number of high-excitation lines including HeII λ 4686. The solid slanted line represents the continuum and is included to reinforce the lack of any bump above noise.

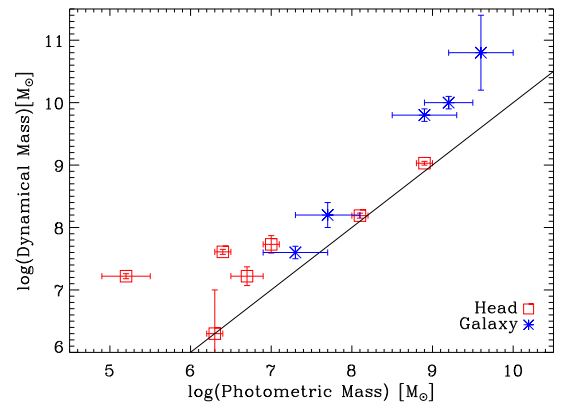


FIG. 9.— Dynamical mass versus photometric mass for the heads of the galaxies (red square symbols) and the full galaxies (blue asterisks). The slanted solid line shows where the two masses are equal. The observed dynamical masses usually exceed the photometric masses. The heads of three tadpoles lie on the equality line within the errors, meaning that their dynamical masses are consistent with their photometric masses.

duces is much too small to account for the >0.5 dex gradients we detect (Fig. 10). Sánchez Almeida et al.

(2009, Appendix A) studied the difference between the oxygen abundance derived from the direct method and

from N2 in a large set starburst galaxies with spectra similar to our tadpoles. There were no systematic differences within 0.2 dex for $12 + \log(\text{O}/\text{H}) \geq 7.7$, which secures the reliability of the abundances found in most locations. As for the points with $12 + \log(\text{O}/\text{H}) \simeq 7.5$, N2 overestimates the oxygen abundance, which again secures the low metallicity values we find. Since N2 provides the O metallicity based on the flux of a N line, the metallicity may be biased in objects with unusual N/O. The effect of varying N/O seems to be unimportant too. Figure 11, shows the ratio as derived from $[\text{SII}]\lambda 6717, 6731/[\text{NII}]\lambda 6583$ – Eq. (11). (The [SII] lines are not available in two targets and therefore we cannot estimate their N content.) Even though the error bars are large, the observed N/O looks rather constant along the galaxies, at approximately the plateau typical of low metallicity galaxies ($\log(\text{N}/\text{O}) \simeq -1.5$; e.g., Pérez-Montero & Contini 2009). Obviously, if N/O is constant then it cannot fake the observed metallicity drop. However, since the error bars of N/O are large, we decided to run a chi-squared test (e.g., Press et al. 1986) to further discard N/O as the source of the measured O variations in KISO5639 and KISO6877. We compared the observed O with the fake variations to be expected if O is constant but N2 varies as N/O in Fig. 11. The test shows how the two variations are inconsistent with 90% confidence.

Figure 12a shows the mass-metallicity relationship for our galaxies, plotting the oxygen abundance of the head versus the photometric mass of the galaxy. The most massive tadpoles tend to have the largest metallicities, although the metallicity values are displaced downward with respect to the mass-metallicity relationship found in the local universe. The dashed line shows the divide above which 97.5 % of the local galaxies are found according to Tremonti et al. (2004). The tadpoles appear just below this line, so they are metal poor for their masses⁶. The mass-metallicity relationship varies with redshift so that the same galaxy mass corresponds to lower oxygen metallicities at higher redshifts (a 0.56 dex drop at redshift 2.3, according to Erb et al. 2006). Our tadpoles are on the mass-metallicity relationship observed at higher redshifts (see the dotted line in Fig. 12a).

We note that the metallicity of the heads also scales with their dynamical masses (Fig. 12b). The relationship is even tighter than the relationship with galaxy photometric mass (Fig. 12a), but we do not have enough points to judge whether or not the improvement is statistically significant. From a practical point of view, the reduction of scatter associated with the use of dynamical masses supports the reliability of our estimate of this physical parameter.

8. NOTES ON INDIVIDUAL GALAXIES

The general properties of the sample are discussed in detail in the preceding sections. Here we focus on a few specifics of the individual galaxies.

⁶ As we already pointed out, the metallicity scale is not free from uncertainties. However, even taking them into account, the tadpoles are metal poor. The triple-dotted dashed line in Fig. 12a shows the solid line transformed to our metallicity scale using the prescription by Kewley & Ellison (2008). The observed metallicities are well below this line too.

KISO3193. This is the only tadpole that shows no rotation, and its line-width versus position curve has a curious double-hump shape (Fig. 5). Its light distribution is less lopsided than for the other tadpoles (Figs. 1 and 4). The absence of rotation combined with the increase of linewidth toward the outskirts and the mild lopsidedness may be consistent with a face-on disk, and in this sense KISO3193 differs from the rest of the sample. The observed linewidths are fairly large, comparable to those of other larger galaxies in the sample. Consequently, the dynamical mass of the head inferred from linewidths is significantly larger than its stellar (photometric) mass.

KISO3867. In both mass and size, this is the smallest tadpole in the sample (see the photometric masses of the full galaxies in Table 2, and also the 1kpc scales given in Fig. 4). Its linewidths do not differ so much from the linewidths of other tadpoles, which contrasts with the low photometric mass inferred in Paper I for the head of the tadpole. Consequently, the ratio of dynamical mass to photometric mass is particularly high in this case – the dynamical mass of the head turns out to be a hundred times larger than the stellar mass derived from photometry (Table 2). The comparatively large oxygen abundance we derive for the head ($12 + \log(\text{O}/\text{H}) \simeq 8$) is probably an overestimate due to observational errors. A few pixels away from the head the abundance drops by 0.3 dex (Fig. 10), which would bring the galaxy down to a more natural location in the mass-metallicity relationship (Fig. 12a).

KISO5149. The asymmetry of its RC is remarkable: see Fig. 3. It extends much further out to one side, which would imply that half of the disk is missing from observation. We cannot explain how this happens, unless the galaxy has a cigar-like shape rather than an axisymmetric structure. It is unlikely that large reddening obscures half the disk, since the SDSS image does not show a large color gradient across the galaxy. It may be a merger, but then it would have to produce an unlikely large scale velocity field resembling a RC. The oxygen abundance is fairly constant along the galaxy, which seems to be associated with being a massive object (it has the largest mass of the sample – Table 2). The galaxy presents a second bright knot separated from the rotation center.

KISO5639. It is one of the XMP galaxies in the sample, with the head being a young starburst (a few Myr old). It also presents a very irregular RC, particularly in the outer parts.

KISO6669. This galaxy has a second bright knot, not far from the head (Fig. 4). The two knots are of low metallicity, which contrasts with the metallicity of the rest of the galaxy (Fig. 10). The center of the RC stays in between the two emission peaks of the galaxy (and so, off-centered; see Fig. 3). The linewidth curve shows a significant dip which does not coincide with any of the two emission peaks (Fig. 5).

KISO6877. This tadpole has the lowest metallicity and is the youngest object in the sample, and its bright head does not seem to contain dark matter. It also presents unusual high-excitation emission lines in the spectral region of the WR bumps (Sect. 5). As we explain in Sect. 6,

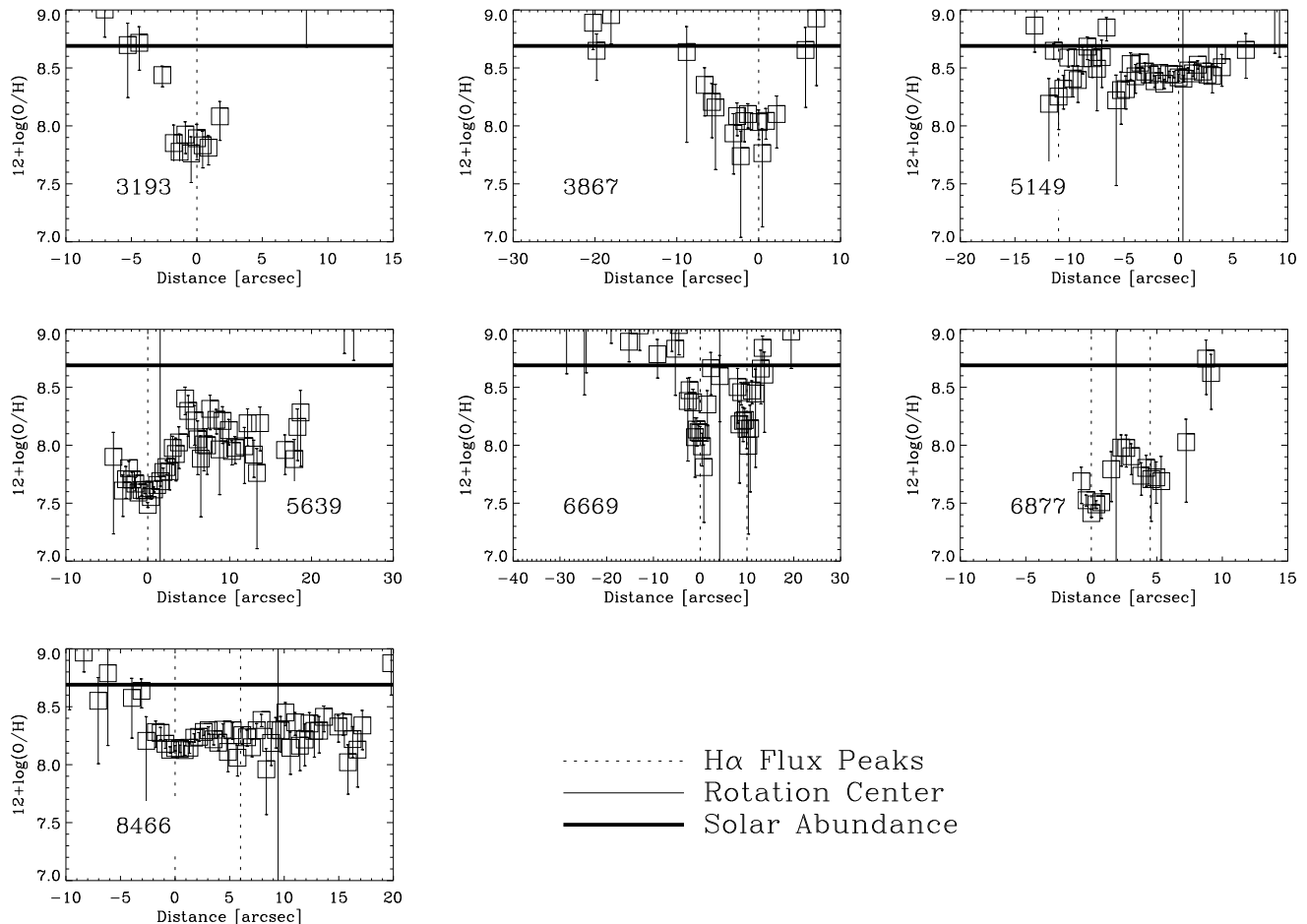


FIG. 10.— Oxygen abundance variation across the galaxies. The vertical solid line represents the center of rotation, whereas the vertical dotted lines indicate the location of maxima in the $H\alpha$ flux profile. The thick horizontal solid line indicates the solar metallicity (from Asplund et al. 2009). Note the existence of abundance variations, with the minima coinciding with the largest $H\alpha$ signals. Note also that KISO5639 and KISO6877 reach very low abundances, below one-tenth of the solar value, therefore, they are members of the set of rare XMP galaxies. The sorting of the galaxies and the abscissae are identical to those in Fig. 3.

we sought distortions in the RCs that could be associated with massive self-gravitating heads. Perhaps KISO6877 represents the only example. Although we cannot assess the reliability of the distortion present in its RC at the head position (see Fig. 3), we carried out the academic exercise of reproducing the observed velocity curve with two RCs combined, one for the galaxy plus one for the head. The center of rotation of the head has been forced to be given by the position of the head. The combined RC is shown as the dashed line in Fig. 13, and it improves the fit to the data points (compare with the solid line). The head is modeled with a counter-rotating disk with a maximum velocity of 6 km s^{-1} , which according to Eq. (5) corresponds to a dynamical mass of $\log(M/M_\odot) \simeq 6.7$. The mass thus derived is similar to both the photometric mass of the head and the dynamical mass inferred from linewidth (see Table 2). We also note the coincidence of this wiggle in the RC with an obvious decrease in line-width associated with the head (see Fig. 5).

KISO8466. The galaxy has a multi hump structure (Fig. 1 and 4). The line-width curve presents a curious two-hump shape, which is not centered in photometric

maxima (Fig. 5). The oxygen metallicity is rather uniform along the galaxy, as for the other massive galaxy in the sample, KISO5149.

9. DISCUSSION AND CONCLUSIONS

Galaxies with a bright peripheral clump on a fainter tail are called cometary or tadpole (Fig. 1). The origin of the shape is unknown, but it may trace a transit phase in the assembly of many disk galaxies (Sect. 1). Low mass local tadpoles were identified and studied photometrically in Paper I. Here we follow up the study, and analyze the chemical and dynamical properties of seven such targets inferred from long-slit spectra around $H\alpha$.

Five out of the seven observed tadpoles show evidence for rotation ($\sim 70\%$), and a sixth target hints at it. Often the center of rotation is spatially offset with respect to the tadpole head (three out of five cases). The RCs of the smaller targets are not smooth but present fluctuations, suggesting a complex dynamics (e.g., a counter-rotating head – see Fig. 13). The size and velocity dispersion of the heads are typical of giant HII regions and follow the scaling relationship known to exist between these two quantities (Fig. 6). We find changes of velocity dispersion along the galaxies, but they are not correlated with

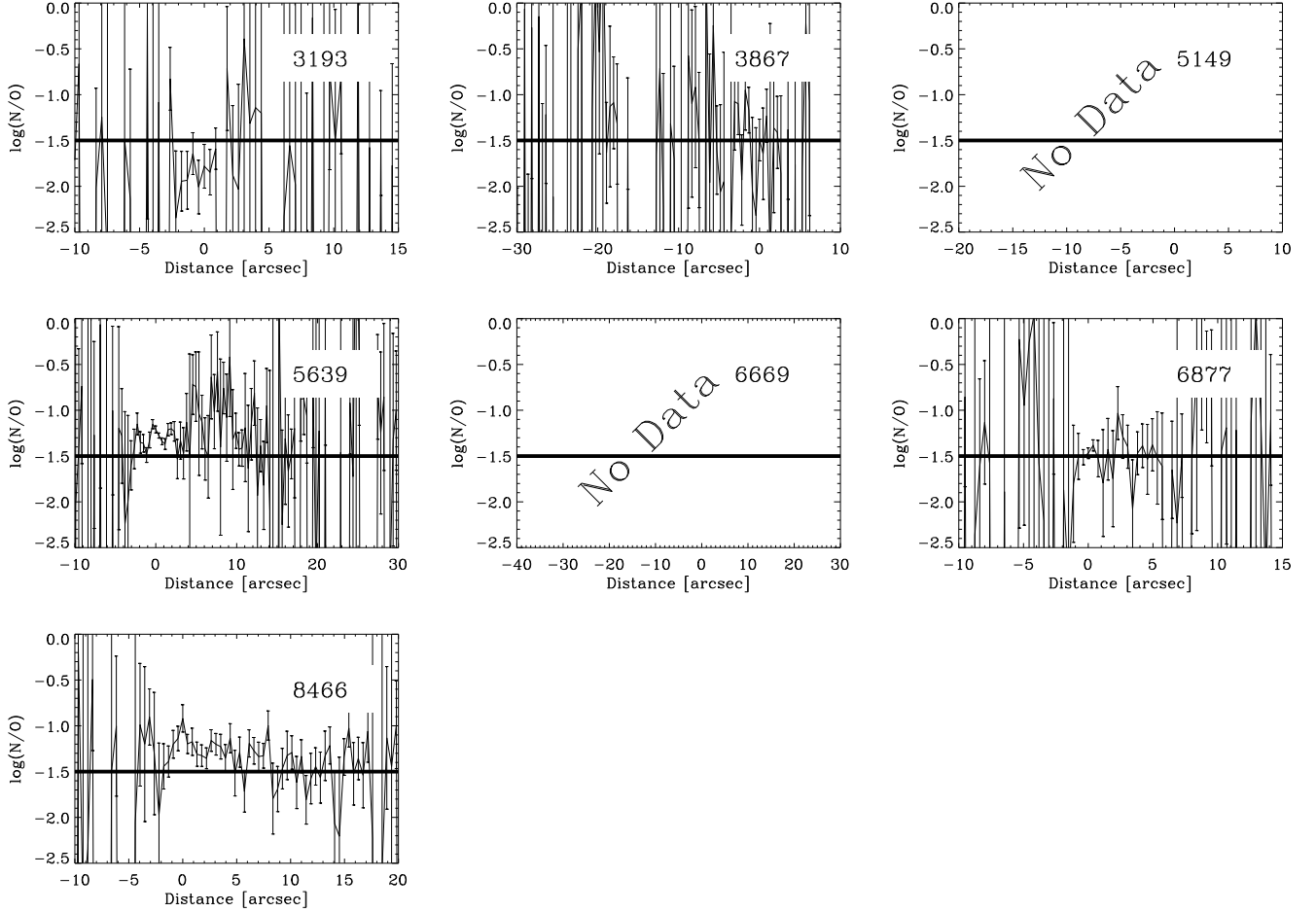


FIG. 11.— Variation of the ratio N to O across the galaxies. The horizontal solid line represents the plateau at some $\log(N/O) \simeq -1.5$ found in most low metallicity galaxies, for which N is produced as a primary element. The sorting of the galaxies and the abscissae are identical to those in Fig. 3. The ratio could not be estimated in the two galaxies of largest redshift, where the required emission lines lie outside the observed spectral range.

intensity variations. If anything, there is a tendency for the tadpole heads to coincide with local minima of velocity dispersion. The head is defined as the position on the galaxy with the largest surface brightness. Observationally, we find it to coincide with the region of largest $H\alpha$ flux, and so, of largest SFR in the galaxy (e.g., Kennicutt 1998). Moreover, we also find the continuum flux to extend further out as compared to the flux in $H\alpha$, which is concentrated around the head. Thus the bright heads seem to be large starbursts with their random motions reduced with respect to the rest of the galaxy.

Using the observed RCs and velocity dispersions, we estimate the dynamical masses of the galaxies and their heads. The dynamical masses of the full galaxies are between three and ten times larger than the stellar mass inferred from photometry. The dynamical masses of the heads also exceed their stellar masses, but to a lesser extent than the full galaxies. Actually, the photometric mass and the dynamical mass of three heads agree within error bars. In two other cases, however, the dynamical mass of the head exceeds the photometric mass of the full galaxy.

The oxygen metallicity estimated from $[NII]6583/H\alpha$ often shows significant spatial gradients across the galax-

ies (~ 0.5 dex), being lowest at the head and increasing in the rest of the galaxy, tail included. So far as we are aware of, this is the first time that a metallicity growing away from HII regions has been reported in local galaxies. The sense of the resulting metallicity gradient is at variance with the observation of local disk galaxies, where the gas-phase metallicity increases toward the galaxy centers (Vilchez et al. 1988; Garnett et al. 1997) or is just constant (Moran et al. 2012). However, the type of variation we measure, with a minimum metallicity at the most intense star-forming region, has been observed in galaxies at redshift around 3 by Cresci et al. (2010) where it is interpreted as evidence for infall of pristine gas triggering star formation. Once systematic errors are disregarded (as we did in Sect. 7), it is difficult to avoid such interpretation, also in the case of our tadpole galaxies. We considered and then discarded the following two possibilities: (1) assume a regular metallicity distribution decreasing outward. If the head was formed from gas in the galaxy outskirts, but has spiraled in toward the center by dynamical friction (e.g., Elmegreen et al. 2012a), then the head would naturally present a metallicity lower than its immediate surroundings and similar to the galaxy outskirts. However, this prediction of metallicity gradients

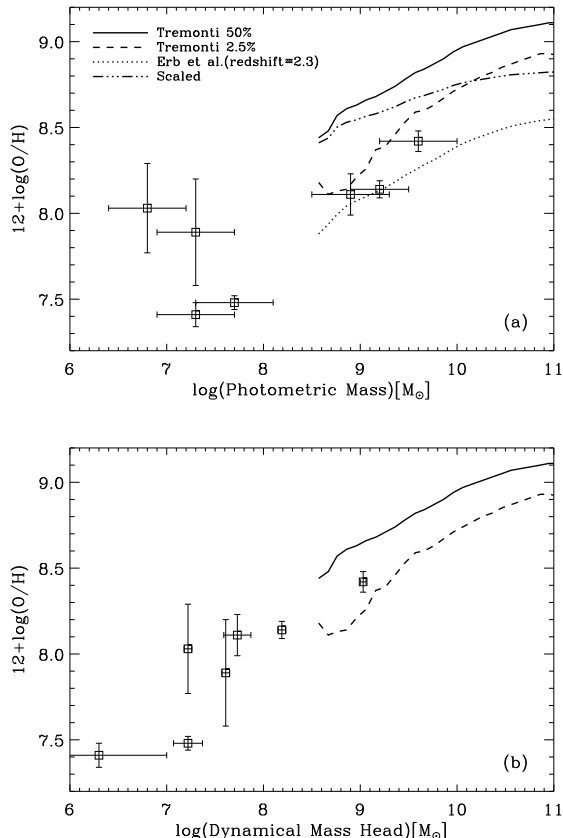


FIG. 12.— (a) Mass metallicity-metallicity relationship for the galaxies. We consider the photometric mass of the galaxy and the oxygen abundance at the galaxy head. The mean relationship found in the local universe by Tremonti et al. (2004) is shown as the solid and the dashed lines – the thick solid line represents the mean of the distribution, whereas the dashed line indicates the line above which 97.5 % of the local galaxies are found. Our targets are outliers of the local relationship; too metal poor for their masses. They are more in the line of the starburst galaxies found at high redshift (the dotted line, from Erb et al. 2006). The triple-dotted dashed line corresponds to the solid line transformed to our metallicity scale using the prescription by Kewley & Ellison (2008). (b) Same as (a) using the dynamical mass of the heads. The solid and dashed lines are also the same, and have been included for reference.

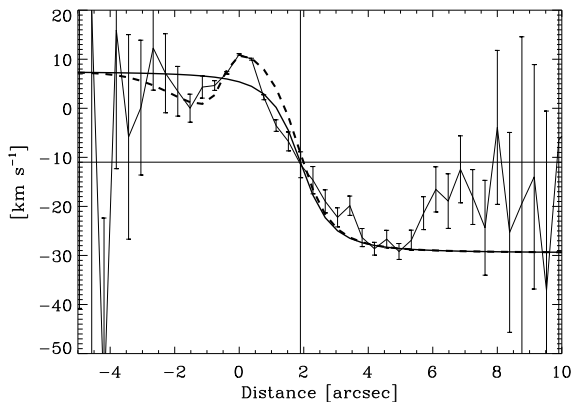


FIG. 13.— Velocity curve of KISO6877 fitted by a single RC (solid line) and including a counter-rotating disk at the position of the head (dashed line). The data points and the solid line are identical to those in Fig. 3.

induced by internal migration is inconsistent with our observation, where the metallicity at the head is not just lower than the surroundings but the lowest (see Fig. 10). (2) Metal-rich supernova (SN) driven winds remove metals from shallow gravitational potential wells, producing metal-poor galaxies (e.g., Mac Low & Ferrara 1999; Recchi et al. 2004). This mechanism explains the overall low gas metallicity of some galaxies with significant old stellar populations, but it does not account for the presence of a region like the tadpole head, with metallicity lower than the rest of the galactic gas. The metals ejected by the winds are those created by the stars that explode as SNe. They are not the metals of the ambient gas. Then the loss of these ejecta reduces the efficiency of the galaxy to retain metals, but it does not reduce the metallicity of a particular region of the galaxy. In short, the interstellar medium of the tadpole galaxies is not well mixed but shows significant metallicity gradients. Since the mixing time scale is expected to be relatively short (shorter than a few Myr; e.g., Tenorio-Tagle 1996; de Avillez & Mac Low 2002), the recent infall of metal-poor gas seems to be the only viable alternative to explain the metallicity drop observed at the tadpole heads.

The observationally motivated interpretation of external gas infall fits in well the cold-flow gas accretion scenario arising from cosmological numerical simulations (e.g., Kereš et al. 2005; Dekel et al. 2009). It predicts localized accretion in clumpy streams of pristine gas ready to create stars. The streams may directly form giant clumps that we detect as tadpole heads or, alternatively, feed the disks with turbulent gas that eventually fragments into giant clumps by gravitational instability. In both cases the massive clumps are prone to migrate toward the galaxy centers and become progenitors of central spheroids (Elmegreen et al. 2008; Ceverino et al. 2010). Other details of the observed tadpole properties are also consistent with the cold-flow accretion scenario. The process is expected to be ubiquitous at high redshift. Then the flows fade away gradually in a process that has not been completed in small galaxies yet (e.g., Kereš et al. 2009). This prediction is consistent with the absence of low metallicity HII regions in large local spirals, as well as in our most massive tadpoles (KISO5149 and KISO8466; see Fig. 10), for which the infall would be already over. The metallicity drop is observed only in the low mass objects, reflecting the downsizing process in galaxy formation.

The geometrical displacement of some of the tadpole heads with respect to the centers of rotation also favors the cold-flow scenario. The expected streams of cold gas never end up at the galaxy center. The clumps are formed in the disk, and require time to be transported inward.

Extremely metal poor (XMP) galaxies are rare. Tadpole galaxies are also rare. The fact that we observe two XMP galaxies in a sample of seven tadpoles cannot be casual (Sect. 10). It is known that a significant fraction of XMP galaxies turns out to be tadpole or cometary (Papaderos et al. 2008; Morales-Luis et al. 2011). Here we find the reverse to be true as well, i.e., tadpoles have a significant chance of being XMP. The coincidence of these two seemingly disconnected properties is best understood if the objects are primitive, with the cometary

shape and the low metallicity reflexing dynamical and chemical youth, respectively.

All these results combined are consistent with the local tadpole galaxies being turbulent disks in early stages of assembling. Their star formation seems to be sustained by accretion of external metal-poor gas.

Thanks are due to R. Amorín, J. Rodríguez Zaurín, R. Sánchez-Janssen, G. Stinson, R. Terlevich, J. Vilchez and E. Wisnioski for enlightening discussions and suggestions on various aspects of the work. Thanks are also due to the anonymous referee for comments that help improving the presentation and the discussions in the paper. A. Varela kindly provided the values for the seeing during observation included in Table 1. This work has been partly funded by the Spanish Ministry for

Science, project AYA 2010-21887-C04-04. JSA, CMT and JMA are members of the Consolider-Ingenio 2010 Program, grant MICINN CSD2006-00070: First Science with GTC. The article is partly based on observations made with the telescopes INT and NOT operated at the Spanish *Observatorio del Roque de los Muchachos* (ORM). KISO5639 and KISO6669 were observed through the NOT Fast-Track Service Program, whereas KISO6877 corresponds to Spain Service Time at ORM. The instrument ALFOSC is provided by the Instituto de Astrofísica de Andalucía (IAA) under a joint agreement with the University of Copenhagen and NOTSA. Funding for SDSS, SDSS-II, and SDSS-III has been provided by the Alfred P. Sloan Foundation, the Participating Institutions, the National Science Foundation, and the U.S. Department of Energy Office of Science.

REFERENCES

- Abazajian, K. N., Adelman-McCarthy, J. K., Agüeros, M. A., et al. 2009, *ApJS*, 182, 543
- Andersen, T. B. 1985, Optical specifications and performance of the Nordic 2.5 M Telescope
- Asplund, M., Grevesse, N., Sauval, A. J., & Scott, P. 2009, *ARA&A*, 47, 481
- Baldwin, J. A., Spinrad, H., & Terlevich, R. 1982, *MNRAS*, 198, 535
- Balthasar, H., Thiele, U., & Woehl, H. 1982, *A&A*, 114, 357
- Bosch, G., Terlevich, E., & Terlevich, R. 2009, *AJ*, 137, 3437
- Boselli, A., Boissier, S., Cortese, L., & Gavazzi, G. 2008, *ApJ*, 674, 742
- Bournaud, F. & Elmegreen, B. G. 2009, *ApJ*, 694, L158
- Brinchmann, J., Kunth, D., & Durret, F. 2008, *A&A*, 485, 657
- Campos-Aguilar, A., Moles, M., & Masegosa, J. 1993, *AJ*, 106, 1784
- Ceverino, D., Dekel, A., & Bournaud, F. 2010, *MNRAS*, 404, 2151
- Ceverino, D., Dekel, A., Mandelker, N., et al. 2012, *MNRAS*, 420, 3490
- Chung, A., van Gorkom, J. H., Kenney, J. D. P., Crawl, H., & Vollmer, B. 2009, *AJ*, 138, 1741
- Corbin, M. R., Vacca, W. D., Hibbard, J. E., Somerville, R. S., & Windhorst, R. A. 2005, *ApJ*, 629, L89
- Cresci, G., Mannucci, F., Maiolino, R., et al. 2010, *Nature*, 467, 811
- Crowther, P. A. 2007, *ARA&A*, 45, 177
- Dalcanton, J. J. & Stilp, A. M. 2010, *ApJ*, 721, 547
- de Avillez, M. A. & Mac Low, M.-M. 2002, *ApJ*, 581, 1047
- Dekel, A., Birnboim, Y., Engel, G., et al. 2009, *Nature*, 457, 451
- Denicoló, G., Terlevich, R., & Terlevich, E. 2002, *MNRAS*, 330, 69
- D’Onghia, E., Vogelsberger, M., Faucher-Giguere, C.-A., & Hernquist, L. 2010, *ApJ*, 725, 353
- Elmegreen, B. G., Bournaud, F., & Elmegreen, D. M. 2008, *ApJ*, 688, 67
- Elmegreen, B. G. & Elmegreen, D. M. 2010, *ApJ*, 722, 1895
- Elmegreen, B. G., Zhang, H.-X., & Hunter, D. A. 2012a, *ApJ*, 747, 105
- Elmegreen, D. M., Elmegreen, B. G., Marcus, M. T., et al. 2009, *ApJ*, 701, 306
- Elmegreen, D. M., Elmegreen, B. G., Ravindranath, S., & Coe, D. A. 2007, *ApJ*, 658, 763
- Elmegreen, D. M., Elmegreen, B. G., Sánchez Almeida, J., et al. 2012b, *ApJ*, 750, 95
- Erb, D. K., Shapley, A. E., Pettini, M., et al. 2006, *ApJ*, 644, 813
- Förster Schreiber, N. M., Genzel, R., Lehnert, M. D., et al. 2006, *ApJ*, 645, 1062
- Franx, M., Illingworth, G. D., Kelson, D. D., van Dokkum, P. G., & Tran, K.-V. 1997, *ApJ*, 486, L75
- Fuentes-Masip, O., Muñoz-Tuñón, C., Castañeda, H. O., & Tenorio-Tagle, G. 2000, *AJ*, 120, 752
- Garnett, D. R., Shields, G. A., Skillman, E. D., Sagan, S. P., & Dufour, R. J. 1997, *ApJ*, 489, 63
- Genel, S., Naab, T., Genzel, R., et al. 2012, *ApJ*, 745, 11
- Genzel, R., Burkert, A., Bouché, N., et al. 2008, *ApJ*, 687, 59
- Guseva, N. G., Papaderos, P., Izotov, Y. I., et al. 2003, *A&A*, 407, 105
- Immeli, A., Samland, M., Westera, P., & Gerhard, O. 2004, *ApJ*, 611, 20
- Izotov, Y. I. & Thuan, T. X. 2004, *ApJ*, 616, 768
- Kehrig, C., Oey, M. S., Crowther, P. A., et al. 2011, *A&A*, 526, A128
- Kennicutt, Jr., R. C. 1998, *ARA&A*, 36, 189
- Kereš, D., Katz, N., Fardal, M., Davé, R., & Weinberg, D. H. 2009, *MNRAS*, 395, 160
- Kereš, D., Katz, N., Weinberg, D. H., & Davé, R. 2005, *MNRAS*, 363, 2
- Kewley, L. J. & Ellison, S. L. 2008, *ApJ*, 681, 1183
- Kunth, D. & Östlin, G. 2000, *A&A Rev.*, 10, 1
- Laing, R. & Jones, D. 1985, *Vistas in Astronomy*, 28, 483
- Leitherer, C., Schaerer, D., Goldader, J. D., et al. 1999, *ApJS*, 123, 3
- Lin, D. N. C. & Faber, S. M. 1983, *ApJ*, 266, L21
- López-Sánchez, Á. R., Koribalski, B. S., van Eymeren, J., et al. 2012, *MNRAS*, 419, 1051
- Mac Low, M.-M. & Ferrara, A. 1999, *ApJ*, 513, 142
- MacAlpine, G. M. & Lewis, D. W. 1978, *ApJS*, 36, 587
- Martin, B. R. 1971, *Statistics for Physicists* (London: Academic Press)
- Mayer, L., Mastropietro, C., Wadsley, J., Stadel, J., & Moore, B. 2006, *MNRAS*, 369, 1021
- Melnick, J., Tenorio-Tagle, G., & Terlevich, R. 1999, *MNRAS*, 302, 677
- Miyauchi-Isoe, N., Maehara, H., & Nakajima, K. 2010, *Publications of the National Astronomical Observatory of Japan*, 13, 9
- Morales-Luis, A. B., Sánchez Almeida, J., Aguerri, J. A. L., & Muñoz-Tuñón, C. 2011, *ApJ*, 743, 77
- Moran, S. M., Heckman, T. M., Kauffmann, G., et al. 2012, *ApJ*, 745, 66
- Muñoz-Tuñón, C. 1994, *Supersonic motions in giant H II regions.*, ed. G. Tenorio-Tagle, 25
- Noguchi, M. 1999, *ApJ*, 514, 77
- O’dell, C. R. & Townsley, L. K. 1988, *A&A*, 198, 283
- Osterbrock, D. E. 1989, *Astrophysics of gaseous nebulae and active galactic nuclei*
- Pagel, B. E. J. & Edmunds, M. G. 1981, *ARA&A*, 19, 77
- Pagel, B. E. J., Simonson, E. A., Terlevich, R. J., & Edmunds, M. G. 1992, *MNRAS*, 255, 325
- Papaderos, P., Guseva, N. G., Izotov, Y. I., & Fricke, K. J. 2008, *A&A*, 491, 113
- Pérez-Montero, E. & Contini, T. 2009, *MNRAS*, 398, 949
- Pettini, M. & Pagel, B. E. J. 2004, *MNRAS*, 348, L59
- Press, W. H., Flannery, B. P., & Teukolsky, S. A. 1986, *Numerical recipes. The art of scientific computing*
- Recchi, S., Matteucci, F., D’Ercole, A., & Tosi, M. 2004, *A&A*, 426, 37
- Roy, J.-R., Arsenault, R., & Joncas, G. 1986, *ApJ*, 300, 624
- Rozas, M., Richer, M. G., López, J. A., Relaño, M., & Beckman, J. E. 2006, *A&A*, 455, 539
- Salucci, P., Lapi, A., Tonini, C., et al. 2007, *MNRAS*, 378, 41
- Salucci, P. & Persic, M. 1997, in *Astronomical Society of the Pacific Conference Series, Vol. 117, Dark and Visible Matter in Galaxies and Cosmological Implications*, ed. M. Persic & P. Salucci, 1
- Sánchez Almeida, J., Aguerri, J. A. L., Muñoz-Tuñón, C., & Vazdekis, A. 2009, *ApJ*, 698, 1497
- Schaerer, D., Contini, T., & Pindao, M. 1999, *A&AS*, 136, 35
- Shi, F., Kong, X., Li, C., & Cheng, F. Z. 2005, *A&A*, 437, 849
- Shirazi, M. & Brinchmann, J. 2012, *MNRAS*, 421, 1043

- Stoughton, C., Lupton, R. H., Bernardi, M., et al. 2002, *AJ*, 123, 485
- Straughn, A. N., Cohen, S. H., Ryan, R. E., et al. 2006, *ApJ*, 639, 724
- Tenorio-Tagle, G. 1996, *AJ*, 111, 1641
- Terlevich, R. & Melnick, J. 1981, *MNRAS*, 195, 839
- Tremonti, C. A., Heckman, T. M., Kauffmann, G., et al. 2004, *ApJ*, 613, 898
- van den Bergh, S. 1994, *ApJ*, 428, 617
- van Zee, L., Skillman, E. D., & Haynes, M. P. 2004, *AJ*, 128, 121
- Vilchez, J. M., Pagel, B. E. J., Diaz, A. I., Terlevich, E., & Edmunds, M. G. 1988, *MNRAS*, 235, 633
- Windhorst, R. A., Cohen, S. H., Straughn, A. N., et al. 2006, *New Astron. Rev.*, 50, 821
- Wisnioski, E., Glazebrook, K., Blake, C., et al. 2012, *MNRAS*, 422, 3339